

Rationalization of promoted reverse water gas shift reaction by Pt₃Ni alloy: Essential contribution from ensemble effect

Cite as: J. Chem. Phys. **154**, 014702 (2021); <https://doi.org/10.1063/5.0037886>

Submitted: 17 November 2020 . Accepted: 09 December 2020 . Published Online: 04 January 2021

Hong Zhang, Xuelong Wang,  Anatoly I. Frenkel, and  Ping Liu



View Online



Export Citation



CrossMark



New

Your Qubits. Measured.

Meet the next generation of quantum analyzers

- Readout for up to 64 qubits
- Operation at up to 8.5 GHz, mixer-calibration-free
- Signal optimization with minimal latency

[Find out more](#)



Zurich Instruments

Rationalization of promoted reverse water gas shift reaction by Pt₃Ni alloy: Essential contribution from ensemble effect

Cite as: J. Chem. Phys. 154, 014702 (2021); doi: 10.1063/5.0037886

Submitted: 17 November 2020 • Accepted: 9 December 2020 •

Published Online: 4 January 2021



View Online



Export Citation



CrossMark

Hong Zhang,¹ Xuelong Wang,² Anatoly I. Frenkel,^{2,3}  and Ping Liu^{1,2,a)} 

AFFILIATIONS

¹Department of Chemistry, Stony Brook University, Stony Brook, New York 11794, USA

²Chemistry Division, Brookhaven National Laboratory, Upton, New York 11973, USA

³Department of Materials Science and Chemical Engineering, Stony Brook University, Stony Brook, New York 11794, USA

Note: This paper is part of the JCP Special Collection in Honor of Women in Chemical Physics and Physical Chemistry.

a) Author to whom correspondence should be addressed: pingliu3@bnl.gov

ABSTRACT

Bimetallic alloys have attracted considerable attention due to the tunable catalytic activity and selectivity that can be different from those of pure metals. Here, we study the superior catalytic behaviors of the Pt₃Ni nanowire (NW) over each individual, Pt and Ni NWs during the reverse Water Gas Shift (rWGS) reaction, using density functional theory. The results show that the promoted rWGS activity by Pt₃Ni strongly depends on the ensemble effect (a particular arrangement of active sites introduced by alloying), while the contributions from ligand and strain effects, which are of great importance in electrocatalysis, are rather subtle. As a result, a unique Ni–Pt hybrid ensemble is observed at the 110/111 edge of the Pt₃Ni NW, where the synergy between Ni and Pt sites is active enough to stabilize carbon dioxide on the surface readily for the rWGS reaction but moderate enough to allow for the facile removal of carbon monoxide and hydrogenation of hydroxyl species. Our study highlights the importance of the ensemble effect in heterogeneous catalysis of metal alloys, enabling selective binding–tuning and promotion of catalytic activity.

Published under license by AIP Publishing. <https://doi.org/10.1063/5.0037886>

I. INTRODUCTION

Transition metal alloys have been widely used in catalysis, due to the unique and tunable catalytic activity and selectivity that can be different from those of pure metals.¹ In this context, platinum (Pt) alloys attracted considerable attention, being able to well catalyze the electrochemical reactions, e.g., oxygen reduction, hydrogen evolution, and ethanol oxidation.^{2–4} Specifically, alloying Pt with earth-abundant metals can reduce the Pt content of electrocatalysts by increasing their intrinsic activity,⁵ among which Pt–Ni (nickel) alloys were the most extensively studied.^{6–10} Compared to pure Pt, the enhanced oxygen reduction activity of Pt–Ni alloys in the form of both core–shell and well-mixed bulk alloys was attributed to the ligand effect, where the Pt electronic structure was modified due to the formation of Pt–Ni bonds and/or strain effect, where the large lattice mismatch between Pt and Ni introduced

a strong compression to the Pt–Pt bonds and tensile strain on the Pt–Ni bond.^{5,10–12} The ligand effect and strain effect were difficult to separate as they typically were combined to influence the width and position of the d-band,¹³ which further altered the interactions of metal sites, Pt in this case, with the adsorbate molecules significantly, while the Ni site did not participate in the reaction directly.^{5,10–12}

In contrast to the considerable attention paid to Pt–Ni alloys in electrocatalysis, the studies on thermal catalysis were rather limited. Recently, the exceptional catalytic behaviors of Pt–Ni from the individual monometallic systems were reported during CO₂ hydrogenation. Upon exposure to CO₂ and H₂, Pt alone was found to be selective to CO via the reverse Water Gas Shift (rWGS) reaction (CO₂ + H₂ → CO + H₂O), an endothermic reaction that involved activating the CO₂ molecule to CO by hydrogen;^{14,15} yet, it bound CO₂ too weakly. Thus, the stabilization of CO₂ on the surface for

further hydrogenation can be essential to the overall activity.¹⁶ By comparison, Ni bound CO₂ more strongly to facilitate the conversion and the C–O bond breakage. The strong binding provided by Ni also stabilized the adsorbed *CO produced via the rWGS reaction. As a result, the desorption of CO into the gas phase and, thus, the rWGS could not compete with carbon deposition and sintering. For the Ni-rich Pt–Ni alloys, e.g., Pt-doped Ni(111),¹⁷ doping a Pt adatom in the Ni lattice was found to not only facilitate the activation and hydrogenation of CO₂ but also promote *H_xCO hydrogenation to methanol; yet, the methanation and carbon deposition still occurred as seen for Ni alone. In the case of Pt-rich alloys, e.g., Pt₃Ni nanostructure,¹⁵ it behaved similarly to Pt alone, which suggested the rWGS as the dominant pathway with the yield of CH₄ less than 0.1%. The difference was that the CO/CH₄ ratio of Pt₃Ni was 100 higher than that of Pt. Such high CO selectivity and low CH₄ selectivity can be used for the Fischer–Tropsch process to further adjust the CO/H₂ ratio in syngas.¹⁸ The origin of the promoting effect was associated with a nanostructure of the Pt₃Ni intermetallic compound.¹⁵ However, how the Pt–Ni alloy functions to facilitate the selective CO₂ to CO conversion remains elusive at the molecular level. It was hypothesized that the observed superior catalytic performance depended on the intermetallic Pt–Ni sites, as reported previously for the Pt–Ni^{19–21} and Pt–Cu²² single atom alloys (SAAs). The unique ensemble of active sites of SAAs [containing, typically, a dilute (active) metal site and host (inert) metal sites] can behave differently from the other heterometallic sites of metal alloys.²³

In this paper, density functional theory (DFT) calculations were performed to gain a better understanding of the promoting effect by bimetallic Pt₃Ni during the rWGS reaction. To capture the structural characteristics of nanostructures, which had significant effect on the catalytic performances,^{24–29} the nanowire (NW) of Pt₃Ni was considered with the shape of truncated octahedron in the cross section and size of 2 nm in diameter. The Pt and Ni NWs with the same size and shape were also included for comparison. Indeed, the DFT results showed that such a NW model was capable of capturing the local structures at the edges and facets of nanoparticles previously reported.¹⁵ Our studies identified the most active sites and determined the associated energy profiles. More importantly, by analyzing the interplay among ligand, strain, and ensemble (a particular arrangement of active sites) effects, we were able to provide a better understanding of the bimetallic-introduced promoting effect toward the selective rWGS reaction, which can be of great importance to guide the optimization of alloy catalysts.

II. METHOD

Spin-polarized density functional theory (DFT) calculations were performed using the Vienna *Ab initio* Simulation Package (VASP).^{30–32} The Perdew–Burke–Ernzerhof (PBE)³³ functional was used to describe electronic exchange and correlation. The pseudopotential files were prepared using Vaspkit.³⁴ All systems were initialized using the conjugate gradient ionic relaxation algorithm³⁵ and then converged with the RMM-DIIS ionic relaxation algorithm³⁶ with a plane wave cutoff energy of 400 eV. The Brillouin zone was sampled including Γ points. The electronic convergence level of 1×10^{-6} eV was used to obtain the convergence of the electronic structure, and the ionic relaxation was activated and satisfied until the Hellman–Feynman force is less than 0.02 eV/Å on each ion.

Pt, Ni, and Pt₃Ni NWs were constructed based on their face centered cubic (fcc) bulk structures with the optimized lattice constant of 3.98 Å, 3.51 Å, and 3.88 Å, respectively. The NWs were oriented along the (011) direction [Figs. 1(a)–1(c)], so that the most close-packed and stable³⁷ facets were exposed and interconnected by {110} and {100} to form an octahedral shape.³⁸ The size of NWs was about 2 nm in diameter. Under the periodic boundary condition, at least 1.5 nm of vacuum was included perpendicular to the NW direction to avoid lateral interactions between NWs. The NWs were allowed to be fully relaxed with the adsorbate during geometry optimization. Several models of Pt₃Ni NWs were constructed based on the Pt₃Ni bulk alloy. The core of the alloy NW always adopted the bulk structures, while the difference was on the shell, which could be Pt₃Ni bulk-truncated, Pt-rich or Pt skin, or Ni-rich or Ni skin. The results showed that the NW with the bulk-like shell was the most stable and was considered for further calculations on the rWGS reaction [Fig. 1(c)]. The selected Pt₃Ni NW also agreed well with the experimental measurement, showing no Ni–Ni bond was formed.¹⁵

A surrogate Gaussian process regression atomistic model^{39,40} was used to search the transition states (TSs) along with the conventional Nudged Elastic Band (NEB) method. Compared to the conventional NEB method, this Machine Learning Nudged Elastic Band (MLNEB) approach does not need to move and evaluate all images between the reactant and the product together and significantly reduces the time and computing power consumed, while it retains the same level of accuracy as the conventional NEB method.⁴¹ The optimized configurations for the transition state and the other intermediate states served as the initial using the MLNEB method that reoptimized the conventional NEB for final confirmation.

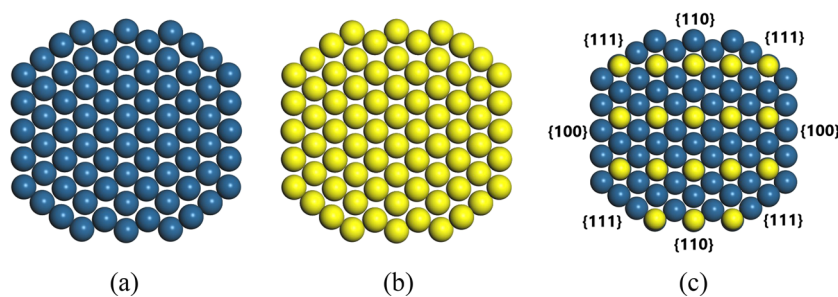


FIG. 1. Optimized structures of intersection for the (a) Pt NW, (b) Ni NW, and (c) Pt₃Ni NW (yellow: Ni; blue: Pt).

III. RESULTS

A. CO adsorption

In our DFT calculations, CO was used as a probing molecule to map the active sites of three NW catalysts: Pt, Ni, and Pt₃Ni NWs. The adsorption energy is determined by $E_{\text{ads}} = E_{\text{CO/NW}} - E_{\text{NW}} - E_{\text{CO}}$, where E is the total energy for CO adsorbed on the NW ($^* \text{CO}$), the bare NW, and CO in the gas phase. More importantly, the CO binding energy was identified previously as an important descriptor that controlled the selectivity of rWGS activity on the Pt-based catalysts.¹⁶ That is, the stronger that CO is chemisorbed, the more difficult the rWGS reaction is due to the endothermicity to release the CO molecule into the gas phase as a product and the facilitated CO hydrogenation to methane, which has less industrial value.

All possible sites on terraces and edges of a NW were tested for CO chemisorption, including top, bridge, and hollow sites (Fig. 2). On all three NWs, CO was found to bind most strongly at the edge of {100} and facet of {111} (100/111 edge in our notation) via a two-fold bridge conformation (Fig. 2), wherein the Pt NW is the most active ($E_{\text{ad}} = -2.16$ eV), which is followed by the Pt₃Ni NW ($E_{\text{ad}} = -2.05$ eV) and Ni NW ($E_{\text{ad}} = -2.01$ eV) in a decreasing sequence. Such a trend in the CO adsorption energy corresponds to a variation in the adsorption site from the Pt–Pt bridge in the Pt NW to the Pt–Pt bridge that strongly interacts with core Ni of the Pt₃Ni NW and Ni–Ni bridge in the Ni NW (Fig. 2). Here, we note that in the case of the Pt₃Ni NW, the Pt–Pt bridge with Ni underneath is more preferential than that with Pt underneath for CO adsorption by 0.07 eV.

Compared to the 100/111 edge, the other sites are less active with the CO adsorption energy higher than -2 eV. Here, the statistics on distribution of active sites and likely the amount of $^* \text{CO}$

on the surface depending on the corresponding adsorption energy was performed, where only the active sites with the CO adsorption energy lower than -1.7 eV were counted (Fig. 3), while the sites that weakly bind CO were excluded in consideration of less sticking possibility on exposure to CO. A change in the trend from the most stable adsorption was observed. Although at the most stable 100/111 edge, the CO–Pt NW interaction is stronger than the CO–Ni NW interaction, the trend is reversed according to the statistics including those on other sites. On the Ni NW, there is a rapid increase in the number of sites and, thus, the sticking probability for $^* \text{CO}$ when moving away from the most stable 100/111 edge to the {111}, {100}, and 110/111 edges, and the adsorption energy is between -2 eV and -1.9 eV (Fig. 3). The majority of $^* \text{CO}$ is likely located on {111} terraces, corresponding to the adsorption energy in the range between -1.9 eV and -1.8 eV, where the high symmetric hollow sites are more favorable than the bridge and top sites. This is followed by a rapid decrease when the binding is higher than -1.8 eV. By comparison, the sites on the Pt NW that provide strong CO binding ($E_{\text{ad}} < -1.8$ eV), e.g., 100/111 edge, are rather limited. The major contribution is from hollow sites and bridge sites on {111} facets corresponding to the adsorption energy in between -1.8 eV and -1.7 eV (Fig. 3). The CO binding properties of the Pt₃Ni NW stay between those of the Pt NW and the Ni NW as seen for the most stable 100/111 edge, where the variation with the CO adsorption energy is less significant than that of the Ni NW and Pt NW. Most of $^* \text{CO}$ likely occupies the {111} terraces and the edges associated with {110}, with the CO adsorption energy between -1.9 eV and -1.7 eV (Fig. 3). According to our DFT calculations, statistically, the trend in the CO binding activity follows a decreasing sequence: Ni NW > Pt₃Ni NW > Pt NW, which agrees well with the estimated trend based on Diffuse Reflectance Infrared Fourier

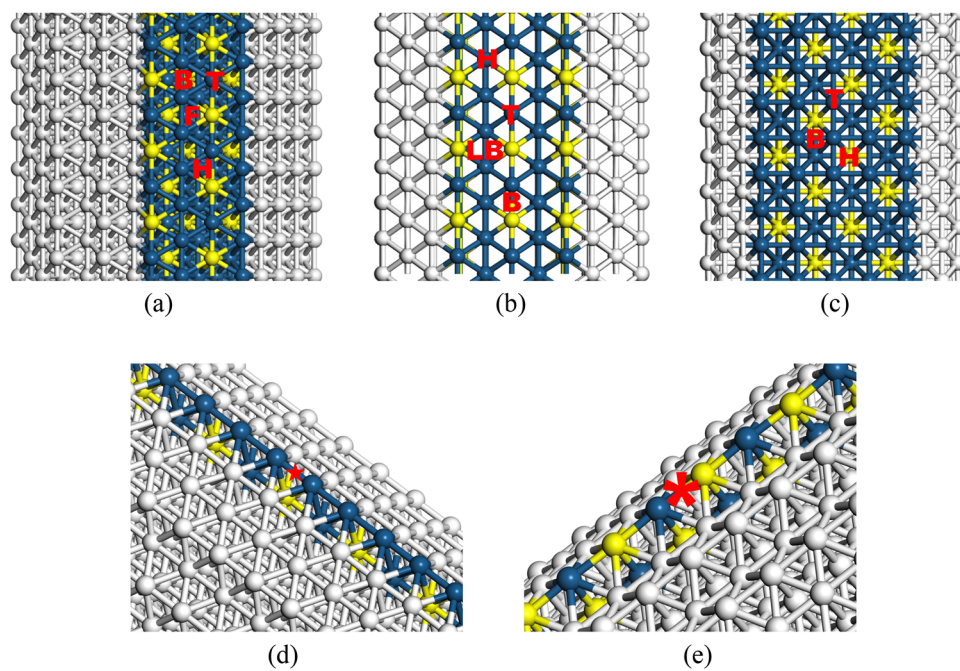


FIG. 2. Views of adsorption sites on the surface of the Pt₃Ni NW. yellow: Ni; blue: Pt; gray: atoms at the neighboring facets and in the (a) {111}, (b) {110}, (c) {100}, (d) {111}/{110}, and (e) {111}/{100} edges (T: top; B: bridge; LB: long bridge; F: fcc; H: hcp; ★: 100/111 edge bridge—most active CO binding site; *: 110/111 edge bridge—most active CO₂ binding site).

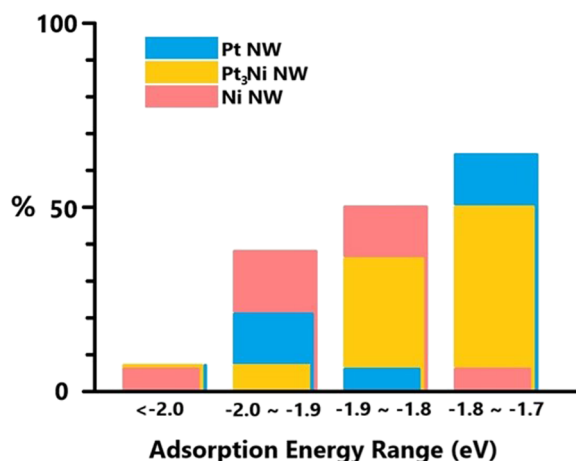


FIG. 3. Statistics on distribution of active sites for CO adsorption on the Pt NW, Ni NW, and Pt₃Ni NW depending on the binding energy.

Transform Spectroscopy (DRIFTS).¹⁵ However, in this case, the statistics do not describe the behavior of the most active sites, which can be more relevant to the catalysis. At the most active 100/111 edge, the CO binding is weakened going from the Pt NW, the Pt₃Ni NW, to the Ni NW.

The preference to the 100/111 edge is associated with the highest-lying d-band with respect to the Fermi level. For instance, according to the calculated partial density of states (PDOS), a similar positive shift in the d-band center (ϵ_d) is observed when going from {111} facets to the 100/111 edge for all NWs studied: ~ 0.13 eV. That is, the 100/111 edge of each NW is more active than the {111} terrace for CO adsorption, by facilitating the electron transfer from the metal to CO and strengthening the CO binding according to the d-band theory.^{42,43} Indeed, as shown in the PDOS, a down-shift of the d-band is observed on the interaction with CO at the most active 100/111 edge of all NWs (Fig. 4). It confirms the dominant back-donation from metal d to CO $2\pi^*$ in the CO adsorption energy as reported previously for metal surfaces.^{42–45} Thus, the higher-lying d-band of metal sites at the 100/111 edge of each NW ensures the stronger CO binding than that of the other sites.

The d-band theory, however, cannot explain the trend in CO adsorption at the most stable 100/111 edge from one NW to the next. The higher-lying Ni d-band of the Ni NW than Pt d of the Pt NW (Fig. 4) does not lead to the enhanced CO binding; instead, the Pt NW is more active (see Sec. III A). The preferential CO adsorption on the Pt NW over the Ni NW at the 100/111 edge is also demonstrated by the larger CO-induced downshift of the d-band center [-0.35 eV, Figs. 4(a) and 4(b)] than that on the Ni NW (-0.09 eV), indicating a more significant electron transfer and, thus, a stronger binding to CO. One of the possibilities for enabling such abnormal behavior can be associated with structural fluxionality of nanostructures, which was reported for Pd@Pt and Ni@Pt core-shell nanoparticles.^{10,25} To demonstrate the local structure of the 100/111 edge, the lattice tension was estimated based on $(d_{M-NW}/d_{M-bulk} - 1) \times 100\%$. Upon CO adsorption, significant changes in the strain of local structures are observed for the Pt NW with the compressed

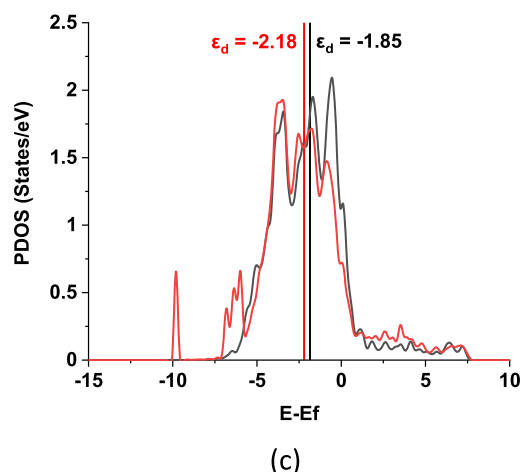
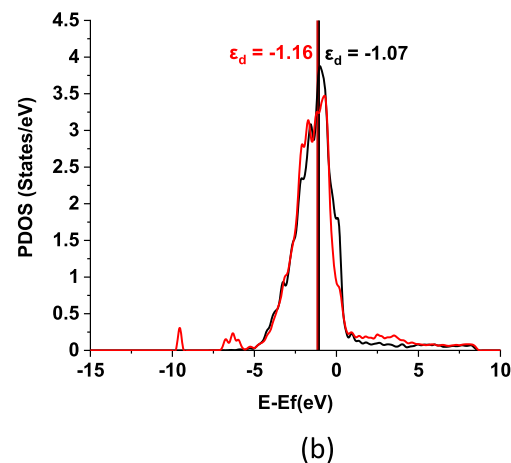
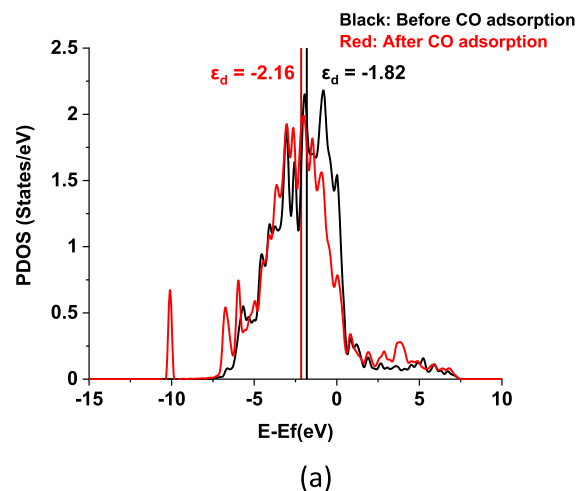


FIG. 4. Partial density of states (PDOS) for Pt 5d or Ni 3d at the most active 100/111 edge of Pt (a), Ni (b), and Pt₃Ni (c) NWs, which interact directly with CO. The PDOSs before and after CO adsorption were included, and the d-band center (ϵ_d) was labeled.

strain released by 1.16% on the surface. By contrast, the variation in strain is 1.00% on the Ni NW. Thus, the 100/111 edge of the Pt NW displays higher structural fluxionality than that of the Ni NW, which allows more distortion in the local structure to accommodate CO molecules better, and this provides stronger binding. Given that, the strain effect, indeed, contributes the binding.

The Pt₃Ni NW always behaves moderately between the Pt NW and the Ni NW. Like the Pt NW, the Pt–Pt bridge site is preferred at the 100/111 edge of the Pt₃Ni NW. As shown in Fig. 4(c), the CO-induced down-shift of Pt 5d is 0.33 eV, which is slightly less than that of the Pt NW but larger than that of the Ni NW. In addition, the higher structural fluxionality of the Pt₃Ni NW enables more significant changes in the local structure on interaction with CO and, thus, stronger CO binding than that of the Ni NW, where the surface contraction strain is released by 1.05%. The weakened Pt–CO binding due to the alloying with Ni is associated with the ligand effect, which leads to the slight downshift in Pt 5d from –2.16 eV for the Pt NW to –2.18 eV according to the d-band theory.

As reported previously,¹⁶ the strong CO binding can hinder CO desorption, enhance CO hydrogenation to methane, and, thus, decrease the CO selectivity via the rWGS reaction. Based on the DFT-calculated CO adsorption energies at the most stable site, it seems that both Ni and Pt₃Ni NWs are more active than the Pt NW toward the rWGS reaction, where Pt likely binds CO too strongly to be removed from the surface.

B. CO₂ adsorption

The chemisorption of CO₂ was also studied. It is particularly important to identify the active sites on NWs, which initiate the rWGS reaction. Similar to the case of CO, all the possible sites on the {100}, {110}, {111} facets and edges of three NWs are tested for CO₂ adsorption (Fig. S1), where the similar structures for the chemisorbed CO₂ (*CO₂) via either $\eta^2_{\text{C,O}}$ or $\eta^3_{\text{C,O,O}}$ conformation were also reported previously on Ni surfaces.⁴⁶ Our DFT calculations reveal that the interaction between CO₂ and Ni NWs is stronger than that with the Pt NW, and the alloy falls in the middle. The most active binding site for CO₂ on all NWs is at the low-coordinated edges, as reported previously on other metal catalysts.^{47,48} On the Pt NW and Ni NW, the 100/111 edge is the most active site for CO₂ adsorption as seen for CO. It is easy to understand the preference to the 100/111 edge, due to the high-lying d-band of associated Pt or Ni (Fig. 4). Again, the Pt–Pt bridge site is preferred on the Pt NW via $\eta^2_{\text{C,O}}$ conformation [Fig. 5(a)], and the

adsorption energy is –0.15 eV (Table S1). On the Ni NW, the favored site slightly shifts from the Ni–Ni bridge to the neighboring hollow site, so that both C and O can be anchored at the Ni bridge site [Fig. 5(b)] to enhance the binding. Compared to the Pt NW, the stronger CO₂ binding of –0.44 eV (Table S1) is observed on the Ni NW. The preference of the CO₂ to the Ni NW over the Pt NW is associated with higher O-affinity of Ni via a higher lying d-band, while the structural fluxionality of the NW does not contribute significantly as seen for CO due to the relatively weak interaction with CO₂. According to the calculated PDOS (Fig. 6), the O atom of *CO₂ is anchored more strongly by Ni at the 100/111 edge of the Ni NW than that of Pt of the Pt NW, which is demonstrated by a larger down-shift in O 2p and more negative charge by 0.38 e according to Bader analysis^{49–51} to gain additional stability.

In the case of Pt₃Ni NW, the most active site for CO₂ adsorption is at the 110/111 edge, specifically the hybrid Pt–Ni bridge site via a SAA motif [Figs. 2 and 5(c)]. It corresponds to the adsorption energy of –0.30 eV (Table S1). The difference between the 110/111 edge and the 100/111 edge is associated with the ensemble effect introduced by alloying. At the 100/111 edge, only Pt atoms are exposed and the Ni atoms are underneath, while both Pt and Ni atoms are located on the surface at the 110/111 edge and each single Ni atom is isolated by Pt neighbors (Fig. 2). The strong O–Ni interaction as seen for the Ni NW results in the variation in adsorption preference to the 110/111 edge on the Pt₃Ni NW (Fig. 6); by comparison via O–Pt interaction, CO₂ is less stable at the 100/111 edge by 0.22 eV (Table S1).

Due to the direct Ni–O bond formation, the Ni NW (C–O bond of 1.39 Å; O–C–O angle to 123°) is more active than the Pt NW (C–O bond of 1.30 Å; O–C–O angle to 130°) to stabilize CO₂, which is demonstrated by a more stretched C–O bond and bent O–C–O angle. The Pt₃Ni NW is an exception. Although the binding energy falls between Pt and Ni NWs, the elongation in the C–O bond is even lightly shorter than that of the Pt NW (C–O bond of 1.28 Å; O–C–O angle to 130°). This seems to be result of the surface rippling by the surface Ni atoms shifted inward due to the shorter Pt–Ni bonds than Pt–Pt bonds. On interaction with CO₂, the strong Ni–O interaction makes the molecule tilt toward the inward Ni atom, which hinders the C–O bond stretching [Fig. 5(c)]. Nevertheless, according to Bader charge, *CO₂ on both the Ni NW (–0.60e) and the Pt₃Ni NW (–0.44e) is more negatively charged than that of the Pt NW (–0.29e), demonstrating the higher degree of CO₂ activation. More importantly, superior stabilization of *CO₂ on the Ni NW and Pt₃Ni NW over the Pt NW may help in hindering

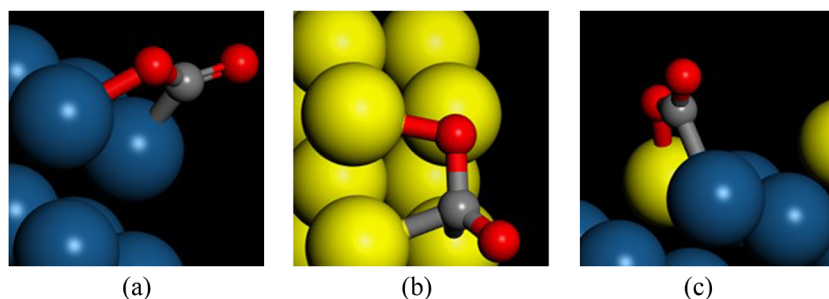


FIG. 5. Optimized local structures for CO₂ adsorption at the 100/111 edge of the Pt NW (a), 100/111 edge of the Ni NW (b), and 110/111 edge of the Pt₃Ni NW (c) (blue: Pt; yellow: Ni; red: O; gray: C).

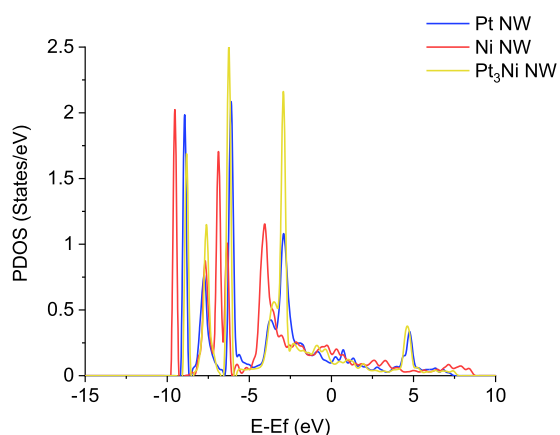


FIG. 6. Partial density of states (PDOS) for O 2p of adsorbed CO₂, which directly interacts with Pt or Ni at the most active 100/111 edge of Pt and Ni NWs and 110/111 edge of the Pt₃Ni NW.

the desorption of CO₂, enabling the sequential activation of CO₂ via C–O bond breaking and, thus, facilitating the overall rWGS reaction.^{16,46}

C. Reverse water gas shift reaction

Based on the calculated adsorption energies of CO and CO₂, the most active edge sites, e.g., 100/111 edge or 110/111 edge, on both Ni and Pt₃Ni NWs likely outperform the Pt NW during the rWGS reaction, being able to provide stronger binding to CO₂, but still weakly binding CO. To validate that, how the three NWs function during

the rWGS reaction is studied using DFT. Here, we note that the dissociative adsorption of H₂ was found to be a very facile step on the (100) and (111) surfaces of both Ni and Pt, and the barrier can be as low as 0.06 eV on Ni and 0.03 eV on Pt surfaces.^{52–55} Accordingly, in our DFT calculations, the H₂ dissociation was not included, but assumed that the dissociated *H fragment is present on the surface. To describe the rWGS reaction, a six-step process was considered by following the previous studies,^{16,56} including (1) CO₂ + * → *CO₂; (2) *CO₂ + *H → *HOCO; (3) *HOCO → *OH + *CO; (4) *OH + *H → *H₂O + *; (5) *H₂O → H₂O + *; and (6) *CO → CO + *.

The rWGS reaction was considered to occur over the most active sites for the adsorption of CO₂: the 100/111 edge on both Pt and Ni NWs (Fig. S2 and Fig. 3) and the 110/111 edge on the Pt₃Ni NW (Fig. 7), which activate the molecule most significantly on interaction or the formation of chemisorbed *CO₂. This is followed by hydrogenation of *CO₂ to *HOCO, which was found as the key intermediate for the rWGS reaction on Pt-based catalysts.¹⁶ Thermodynamics of the *HOCO formation varies depending on the CO₂ binding. By providing the strongest binding to *CO₂, the hydrogenation to *HOCO is endothermic on the Ni NW (reaction energy of 0.06 eV, Fig. 8), while it is exothermic in the case of the Pt NW (reaction energy of –0.03 eV) and Pt₃Ni NW (reaction energy of –0.14 eV). Our calculations show that, kinetically, the presence of the Ni site is of great importance to stabilize the corresponding transition state (TS) by direct participation, where the corresponding barrier increases in a sequence: Ni (barrier of 0.14 eV) < Pt₃Ni (barrier of 0.16 eV) < Pt (barrier of 0.56 eV) (TS1, Fig. 8). Herein, the TS1s for Ni and Pt₃Ni, which are more stable than that of Pt, are characterized by the formation of Ni–O bonds (Fig. S4).

The formed *HOCO undergoes C–O bond cleavage to *CO and *OH, where the corresponding reaction energy differs significantly among three systems. This is due to the preferential binding

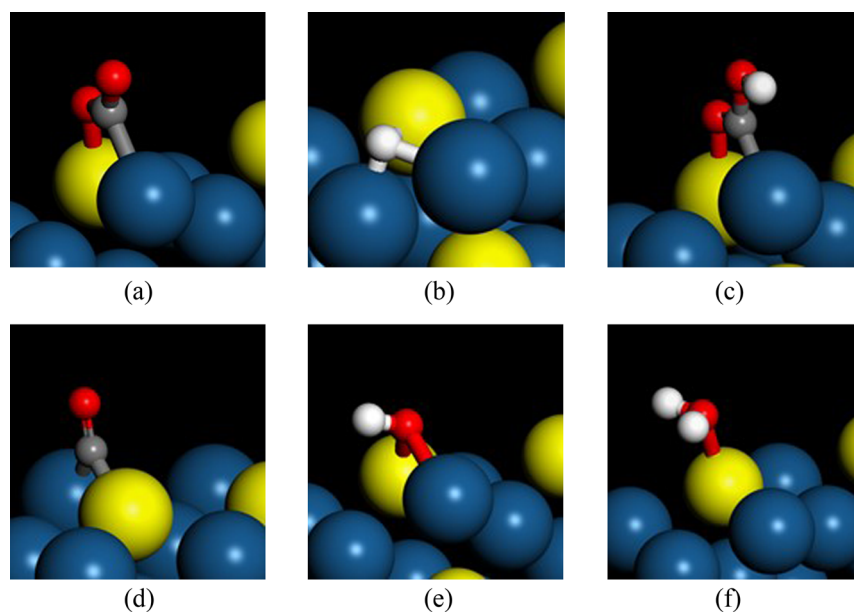


FIG. 7. Optimized structures of the reaction intermediate involved in the rWGS pathway over the 110/111 edge of the Pt₃Ni NW: (a) *CO₂; (b) *H; (c) *HOCO; (d) *CO; (e) *OH; (f) *H₂O (blue: Pt; yellow: Ni; red: O; gray: C; white: H).

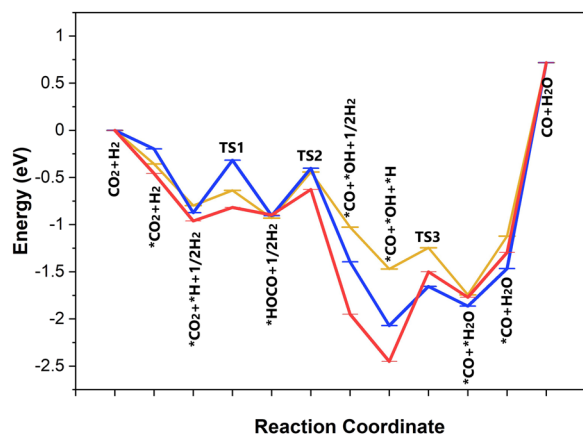


FIG. 8. Potential energy diagram for the rWGS pathway on Pt(blue), Ni(red), and Pt₃Ni(yellow) NWs, where “TS” represents the transition state.

of Ni to the O-containing species. By comparison to CO₂ (Sec. III B), such a preference is more significant to the stronger oxidant. As shown in Fig. 8, the strong binding of *OH at the Ni bridge site of the Ni NW (Fig. S3) drives the high exothermicity for *HOCO dissociation (reaction energy of -1.05 eV), whereas such thermodynamic preference decreases on the Pt NW (reaction energy of -0.48 eV) and Pt₃Ni NW (reaction energy of -0.20 eV). The least exothermicity for the Pt₃Ni NW is attributed to the weakest binding to both *CO and *OH among the three systems (Fig. 8). For *CO, the 100/111 edge of the Pt₃Ni NW is shown to be more active than that of the Ni NW (Sec. III A); however, during the rWGS reaction, the 110/111 edge is the active site due to the preferential CO₂ adsorption. The corresponding CO binding is only -1.82 eV, which is higher than that of Pt and Ni NWs by 0.34 eV and 0.19 eV, respectively. Here, we assume that the diffusion of *CO from the 110/111 edge to the 100/111 edge is very difficult under the reaction conditions. Experimentally, the rWGS reaction was carried out at 673 K,¹⁵ which was likely too low to enable the high mobility of the stable *CO species on the surface. In addition, under the reaction conditions, the CO coverage can be high due to the strong CO–NW interaction, which hinders the diffusion but facilitates the desorption according to the previous studies.^{57–59} In terms of *OH, although the Ni site is available at the 110/111 edge of the Pt₃Ni NW, it is not as active as that of the Ni NW, showing a downshift in the d-band center by 0.03 eV. More importantly, due to the ensemble effect, the highly symmetric Ni hollow sites are not available and *OH is located at the Pt–Ni bridge at the edge (Fig. 7). The corresponding binding is weaker than that in the Ni NW by 0.75 eV and Pt NW by 0.03 eV. Yet, kinetically, the *HOCO dissociation on Pt₃Ni and Pt NWs is very similar to the activation barrier of 0.47 eV and 0.52 eV, respectively, due to the characteristics of early transition (Fig. 8), while the lower barrier on the Ni NW is due to more charge transfer to the adsorbate and elongated C–O bond.

The large difference in the stability of *CO + *OH among the three systems affects the sequential steps along the rWGS pathway significantly. The highly stabilized *OH on the Ni NW hinders the hydrogenation of *OH to *H₂O thermodynamically (reaction

energy of 0.68 eV) and kinetically (barrier of 0.95 eV) more than that of the Pt NW (reaction energy of 0.21 eV; barrier of 0.42 eV) and Pt₃Ni NW (reaction energy of -0.28 eV; barrier of 0.22 eV). That means that the key descriptor for the rWGS on Pt-based catalysts, adsorption energy of CO and CO₂, may not be adequate enough to describe the Ni catalyst, where, besides CO and CO₂, the interaction with *OH should also be taken into consideration. The strong Pt–CO interaction on the Pt NW, on the other hand, imposes a large barrier of 2.16 eV to overcome for desorption, while it is less intense due to the weaker CO binding and, thus, lower barrier on the Ni NW (2.01 eV) and Pt₃Ni NW (1.82 eV). Note that desorption of *CO corresponds to the highest barrier along the rWGS pathway, which is likely difficult to overcome for all three systems even by taking the entropic contributions into consideration, e.g., ~ 1.4 eV at the rWGS temperature of 673 K.¹⁵ However, under the reaction conditions, the coverage of *CO can be higher than that considered in the current DFT calculations. As reported previously for Pt and Ni surfaces or edges,^{57–59} the increase in CO coverage could weaken the binding up to ~ 1 eV and, thus, facilitate the desorption. Nevertheless, the trend in the *CO desorption energy from one system to the next likely remains the same, which is the current interest.

Overall, the DFT calculations show that Pt₃Ni is likely more active than the individual parents for the selective rWGS reaction (Fig. 8), which agrees well with the experimental observation.¹⁵ The variation in the energy along the rWGS on Pt₃Ni is much less than that of the other two systems (Fig. 8). Particularly, the highest barrier along the reaction path for the Pt₃Ni NW is lower than that of Pt and Ni NWs, and thus, the higher activity is expected. Ni is active to stabilize O-containing species, which help stabilize *CO₂ and prevent desorption. The drawback is to bind *OH too strongly to enable facile hydrogenation to water. Pt helps adsorption of the C-anchored species. However, the strong Pt–CO interaction hinders the removal of *CO from the surface, which can undergo further reduction to methanol or methane.^{16,25,60} The promoted rWGS activity by forming the Pt₃Ni alloy is associated with the interplay among the ligand effect, strain effect, and ensemble effect. The ligand effect results in the downshifted d-band for both Ni and Pt sites as compared with that in Ni and Pt alone, which leads to the weakening in binding of reaction intermediates, e.g., *CO and *OH. The strain effect tunes the structural fluxionality on interaction with reaction intermediates and, thus, the binding property, e.g., *CO. Yet, the promotion introduced by forming the Pt₃Ni alloy strongly depends on the ensemble effect, being able to provide the unique Ni–Pt hybrid site with the single Ni atom surrounded by Pt atoms (Figs. 2 and 7). Such a hybrid site takes advantage of the high activity of the Pt site to stabilize the C-anchor and Ni site to stabilize the O-anchor. Consequently, the synergy between Pt and Ni sites at the 110/111 edge enables the selective bond-tuning, being able to bind CO₂ strongly enough to promote the conversion of the rWGS reaction but moderately enough to allow for the facile removal of *CO and hydrogenation of *OH, which is not the case for Pt and Ni.

Our study shows that the tuning effect introduced by forming Pt–Ni alloys in heterogeneous catalysis can be different from that in electrocatalysis. In electrocatalysis, the ensemble effect is limited due to the harsh electrochemical conditions, where Ni atoms in the surface can easily get oxidized and dissolve. Thus, the ligand

effect and mostly strain effect help promote the catalysis. In heterogeneous catalysis, the surface Ni can survive under relatively mild conditions, such as the rWGS reaction in this case. Our study of the Pt₃Ni NW model demonstrated that the formation of intermetallic alloy nanostructures can introduce a unique ensemble on the surface, e.g., Ni single atom isolated by Pt atoms in this case. Such a hybrid site provides selective binding to the reaction intermediates with the direct participation of both Ni and Pt sites. It opens the possibility to move away from the scaling relationship and advance the catalytic activity.

IV. CONCLUSION

The rWGS reaction on Pt₃Ni NWs with octahedral intersection and size of 2 nm was studied using DFT, aiming to understand the underlying mechanism of promoted activity observed previously in the experiment.¹⁵ The individual parent metal NWs of the same size and shape, Pt and Ni, were also included for comparison. Our DFT calculations agreed well with the experimental measurement. Using CO as a probing molecule, the predicted decrease in statistical CO binding going from Ni, Pt₃Ni, to Pt using DFT was consistent with that estimated based on the DRIFTS measurements. More importantly, the measured outperformance of Pt₃Ni over Pt and Ni toward the rWGS was also predicted by the calculation.

The active sites under the rWGS condition were identified based on extensive DFT calculations: 100/111 edge for Pt and Ni NWs and 110/111 edge for the Pt₃Ni NW. In terms of activity, the Ni NW bound *OH too strongly to enable facile hydrogenation to water. The strong Pt–CO interaction hindered the desorption of *CO. The superior rWGS activity of the Pt₃Ni NW over each individual alone strongly depended on the ensemble effect, being able to provide the unique Ni–Pt hybrid site with a single Ni atom surrounded by Pt atoms. The synergy between Pt and Ni sites at the 110/111 edge was active enough to stabilize CO₂ as Ni but moderate enough to allow for the facile removal of *CO and hydrogenation of *OH, which was not the case for Pt and Ni NWs. Our study highlighted the importance of the ensemble effect in heterogeneous catalysis of metal alloys, enabling selective binding–tuning and promotion of catalytic activity.

SUPPLEMENTARY MATERIAL

See the [supplementary material](#) for relevant optimized geometries for reaction intermediates or transition states (Figs. S1–S4) and the calculated adsorption energies (Table S1).

ACKNOWLEDGMENTS

The research carried out at Brookhaven National Laboratory (BNL) was supported by the Division of Chemical Science, Geoscience, and Bioscience, Office of Basic Energy Science of the U.S. Department of Energy (DOE), under Contract No. DE-SC0012704. All the calculations in this work were performed using computational resources at the Center for Functional Nanomaterials (CFN)

and the Scientific Data and Computing Center, a component of the Computational Science Initiative, at BNL under Contract No. DE-SC0012704, at the National Energy Research Scientific Computing Center (NERSC), a DOE Office of Science User Facility, supported by the Office of Science of the DOE under Contract No. DE-AC02-05CH11231, and at Stony Brook University, which was funded by the National Science Foundation under Grant No. 1531492. Investigation of bimetallic alloys by AI Frenkel was supported as part of the Integrated Mesoscale Architectures for Sustainable Catalysis (IMASC), an Energy Frontier Research Center funded by the U.S. Department of Energy, Office of Science, Basic Energy Sciences, under Award No. DE-SC0012573.

DATA AVAILABILITY

The data that support the findings of this study are available from the corresponding author upon reasonable request.

REFERENCES

- 1 J. Greeley and M. Mavrikakis, *Nat. Mater.* **3**, 810 (2004).
- 2 J. Greeley *et al.*, *Nat. Chem.* **1**, 552 (2009).
- 3 L. Zhang and G. Henkelman, *ACS Catal.* **5**, 655 (2015).
- 4 A. Kowal *et al.*, *Nat. Mater.* **8**, 325 (2009).
- 5 S. Liu and P. Liu, *J. Electrochem. Soc.* **165**, J3090 (2018).
- 6 S. Rudi *et al.*, *ACS Catal.* **7**, 6376 (2017).
- 7 X. Huang *et al.*, *Science* **348**, 1230 (2015).
- 8 C. Chen *et al.*, *Science* **343**, 1339 (2014).
- 9 V. R. Stamenkovic *et al.*, *Science* **315**, 493 (2007).
- 10 W. An and P. Liu, *ACS Catal.* **5**, 6328 (2015).
- 11 X. Zhang *et al.*, *J. Chem. Phys.* **142**, 194710 (2015).
- 12 X. Zhang *et al.*, *Phys. Chem. Chem. Phys.* **16**, 16615 (2014).
- 13 J. R. Kitchin *et al.*, *Phys. Rev. Lett.* **93**, 156801 (2004).
- 14 S. Kattel, P. Liu, and J. G. Chen, *J. Am. Chem. Soc.* **139**, 9739 (2017).
- 15 D. Liu *et al.*, *ACS Catal.* **8**, 4120 (2018).
- 16 S. Kattel *et al.*, *J. Catal.* **343**, 115 (2016).
- 17 Z. Ou *et al.*, *Int. J. Hydrogen Energy* **44**, 819 (2019).
- 18 J. Xu and G. F. Froment, *AIChE J.* **35**, 88 (1989).
- 19 M. D. Marcinkowski *et al.*, *Nat. Chem.* **10**, 325 (2018).
- 20 G. Giannakakis, M. Flytzani-Stephanopoulos, and E. C. H. Sykes, *Acc. Chem. Res.* **52**, 237 (2019).
- 21 H. Thirumalai and J. R. Kitchin, *Top. Catal.* **61**, 462 (2018).
- 22 G. Sun *et al.*, *Nat. Commun.* **9**, 4454 (2018).
- 23 P. Liu and J. K. Nørskov, *Phys. Chem. Chem. Phys.* **3**, 3814 (2001).
- 24 S. Cao *et al.*, *Chem. Soc. Rev.* **45**, 4747 (2016).
- 25 W. An and P. Liu, *J. Phys. Chem. C* **117**, 16144 (2013).
- 26 M. Núñez, J. L. Lansford, and D. G. Vlachos, *Nat. Chem.* **11**, 449 (2019).
- 27 Q. Jia *et al.*, *ACS Catal.* **5**, 176 (2014).
- 28 H. Liu *et al.*, *J. Am. Chem. Soc.* **137**, 12597 (2015).
- 29 Z. Zhou *et al.*, *J. Chem. Phys.* **151**, 214704 (2019).
- 30 G. Kresse and J. Furthmüller, *Phys. Rev. B* **54**, 11169 (1996).
- 31 G. Kresse and D. Joubert, *Phys. Rev. B* **59**, 1758 (1999).
- 32 G. Kresse and J. Furthmüller, *Comput. Mater. Sci.* **6**, 15 (1996).
- 33 J. P. Perdew, K. Burke, and M. Ernzerhof, *Phys. Rev. Lett.* **77**, 3865 (1996).
- 34 V. Wang *et al.*, [arXiv:1908.08269](#) (2019).
- 35 W. H. Press *et al.*, *Numerical Recipe* (Cambridge University Press, New York, 1986).
- 36 P. Pulay, *Chem. Phys. Lett.* **73**, 393 (1980).

- ³⁷L. Barrio *et al.*, *J. Phys. Chem. C* **111**, 19001 (2007).
- ³⁸N. A. Lanzillo, *J. Appl. Phys.* **121**, 175104 (2017).
- ³⁹J. A. Garrido Torres *et al.*, *Phys. Rev. Lett.* **122**, 156001 (2019).
- ⁴⁰M. H. Hansen, J. A. G. Torres, P. C. Jennings, Z. Wang, J. R. Boes, O. G. Mamun, and T. Bligaard, [arXiv:1904.00904](https://arxiv.org/abs/1904.00904) (2019).
- ⁴¹O.-P. Koistinen *et al.*, *J. Chem. Phys.* **147**, 152720 (2017).
- ⁴²B. Hammer and J. K. Nørskov, *Adv. Catal.* **45**, 71 (2000).
- ⁴³H. Xin *et al.*, *Phys. Rev. B* **89**, 115114 (2014).
- ⁴⁴A. Ruban *et al.*, *J. Mol. Catal. A* **115**, 421 (1997).
- ⁴⁵I. Takigawa *et al.*, *RSC Adv.* **6**, 52587 (2016).
- ⁴⁶S.-G. Wang *et al.*, *J. Phys. Chem. B* **109**, 18956 (2005).
- ⁴⁷M. J. Hossain, M. M. Rahman, and M. Jafar Sharif, *Nanoscale Adv.* **2**, 1245 (2020).
- ⁴⁸X. Liu, L. Sun, and W.-Q. Deng, *J. Phys. Chem. C* **122**, 8306 (2018).
- ⁴⁹G. Henkelman, A. Arnaldsson, and H. Jónsson, *Comput. Mater. Sci.* **36**, 354 (2006).
- ⁵⁰W. Tang, E. Sanville, and G. Henkelman, *J. Phys.: Condens. Matter* **21**, 084204 (2009).
- ⁵¹M. Yu and D. R. Trinkle, *J. Chem. Phys.* **134**, 064111 (2011).
- ⁵²N. B. Arboleda *et al.*, *Jpn. J. Appl. Phys., Part 1* **46**, 4233 (2007).
- ⁵³P. Kraus and I. Frank, *Int. J. Quantum Chem.* **117**, e25407 (2017).
- ⁵⁴G. Kresse, *Phys. Rev. B* **62**, 8295 (2000).
- ⁵⁵H. Yang and J. L. Whitten, *J. Chem. Phys.* **98**, 5039 (1993).
- ⁵⁶L. C. Grabow *et al.*, *J. Phys. Chem. C* **112**, 4608 (2008).
- ⁵⁷A. Eichler, *Surf. Sci.* **526**, 332 (2003).
- ⁵⁸B. Shan *et al.*, *J. Phys. Chem. C* **113**, 6088 (2009).
- ⁵⁹H. Orita and Y. Inada, *J. Phys. Chem. B* **109**, 22469 (2005).
- ⁶⁰P. Kaiser *et al.*, *Chem. Ing. Tech.* **85**, 489 (2013).